

PACS numbers: 68.37.Hk, 68.37.Ps, 72.40.+w, 78.30.Hv, 78.40.Ha, 78.67.Bf, 88.40.J-

Nanoparticles of Metal Oxide (Bi_2O_3 /PSi/*n*-Si) for Photovoltaic Applications

Hameed H. Ahmed¹, Abdullallah M. Ali¹, and Ahmed N. Abd²

¹*Department of Physics,
College of Education for Pure Sciences,
University of Tikrit,
Tikrit, Salahddin, Iraq*

²*Department of Physics,
College of Sciences
Mustansiriyah University,
Baghdad, Iraq*

Bismuth oxide (Bi_2O_3) nanoparticles are synthesized and evaluated for their function as materials for solar cells. Bi_2O_3 solution is inexpensively produced from the *Nigella sativa* seeds using a green synthetic method. The synthesized Bi_2O_3 solution is deposited by droplet casting method, and the synthesized nanofilm is dried at 80°C. Subsequently, diagnostic tests such as UV–VIS, XRD, and FTIR are performed on the Bi_2O_3 /glass thin films. By means of the SEM, EDS, AFM, and I – V characteristics in dark and under illumination, the optical and structural characteristics of Bi_2O_3 -nanoparticle films are investigated to determine the optical energy gap and crystalline material. X-ray diffraction reveals the presence of a tetragonal crystal system in the phase. The estimated band-gap energy E_g is approximately $E_{g1} = 3.6$ eV, and FTIR analysis shows the degree of infrared absorption as a function of wavelength to demonstrate the presence of functional groups in bismuth-oxide molecules from Bi–O bonds. SEM–EDS morphology studies examine the occurrence of nanocrystals of various shapes and sizes. Finally, as a bulk heterojunction device, the I – V performance of the solar cell (Ag/ Bi_2O_3 /PSi/Si/Ag) deserves attention, and a fill factor $FF = 48$ is found for a solar-cell efficiency of 2.8%, ideality factor $\beta = 1.35$, characterization resistance $R_{CH} = 175 \Omega$, and the parallel resistance = 25.14 Ω .s. This cheap nanoparticle material could be an ideal candidate for future energy applications.

Синтезовано й оцінено наночастинки оксиду Бісмуту Bi_2O_3 на предмет їхньої функції як матеріалів для сонячних елементів. Розчин Bi_2O_3 недорого виробляють з насіння чорнушки посівної зеленим синтетичним методом. Синтезований розчин Bi_2O_3 осаджують методом крапельного

лиття, а синтезовану наноплівку висушують за температури у 80°C. Згодом діагностичні тести, такі як спектрофотометрія в оптичному (видимому) діапазоні з прилеглим до нього ультрафіолетовим діапазоном, рентгенівська дифракція й інфрачервона спектроскопія на основі перетворення Фур'є проводяться на тонких плівках Bi_2O_3 /скло. За допомогою сканувальної електронної мікроскопії, енергодисперсійної рентгенівської спектроскопії, атомно-силової мікроскопії та I - V -характеристик у темряві та за освітлення досліджено оптичні та структурні характеристики Bi_2O_3 -наночастинкових плівок для визначення оптичної енергетичної щільності та кристалічного матеріалу. Рентгенівська дифракція виявляє наявність тетрагональної кристалічної системи в фазі. Розрахункова енергія забороненої зони E_g становить приблизно $E_{g1} = 3,6$ еВ, а аналіза інфрачервоною спектроскопією на основі перетворення Фур'є показує ступінь поглинання інфрачервоного випромінювання як функцію довжини хвилі, щоб продемонструвати наявність функціональних груп у молекулах оксиду Бісмуту з хемічних зв'язків Bi-O . Дослідження морфології за допомогою сканувальної електронної мікроскопії й енергодисперсійної рентгенівської спектроскопії вивчають появу нанокристалів різних форм і розмірів. Нарешті, як пристрій з об'ємним гетеропереходом, експлуатаційні якості I - V сонячного елемента ($\text{Ag}/\text{Bi}_2\text{O}_3/\text{PSi}/\text{Si}/\text{Ag}$) заслуговують на увагу, а коефіцієнт заповнення $FF = 48$ знайдено для ефективності сонячної комірки у 2,8%, коефіцієнт ідеальності $\beta = 1,35$, характеристичний опір $R_{CH} = 175$ Ом і паралельний (шунтувальний) опір = 25,14 Ом·с. Цей дешевий наночастинковий матеріал може стати ідеальним кандидатом для майбутніх енергетичних застосувань.

Key words: biosynthesis, Bi_2O_3 nanoparticles, *Nigella sativa*, drop casting technique.

Ключові слова: біосинтеза, наночастинки Bi_2O_3 , чорнушка посівна, технологія краплинного лиття.

(Received 14 July, 2023; in revised form, 29 August, 2023)

1. INTRODUCTION

Nanomaterials are particles with diameters ranging from 1 nm to 100 nm. Their utility in many practical applications is attributable to the fact that they have various uncommon properties as opposed to larger-size materials [1, 2]. Nano-metal oxides are often utilized in optics, electronics, and catalysts [3]. Many physical and chemical processes have been used to manufacture Nano-metal oxides, which generally include pollutants and poisonous compounds and are hazardous to humans and the environment, as well as taking a long time and consuming a lot of energy, in addition to being unstable and producing by-products. Therefore, it becomes important to shift

to simpler, more environmentally friendly, and ecosystem-friendly manufacturing methods, such as green synthesis techniques [4]. The technology is characterized by the ability to generate stable products with high oxygen content, while the phenolic plant extracts act to oxidize and reduce metal salts and nitrates to nanoscale oxides resulting in more efficient sites with high surface area [5]. The oxide Bi₂O₃ produced in this study can be obtained easily and inexpensively using rice seeds.

2. EXPERIMENTAL DETAILS

Bi₂O₃ is a substantial *p*-type semiconductor with direct optical band gaps of 2.6 eV [6]. Bi₂O₃ thin films are of importance because they have significant traits and properties such as optical energy gap, refractive index, optical conductivity, and mechanical strength [7]. Bismuth oxide, with the formula Bi₂O₃ and the appearance of a yellow crystallite, is a significant material in many technical applications. Powder is distinguished by its colourlessness and tremendous solidity. Bismuth oxide crystals have vital applications in electromagnetic applications and the investigation of optical conductivity of thin films [8]. Bismuth oxide crystals can be made in numerous ways, including thermal oxidation in the air by heating bismuth nitrate at a temperature of 80°C or through green synthesis, which was employed in our study.

3. PREPARATION OF THE PLANT EXTRACT

It also contains pentacyclic soluble in water plant extract of plant seeds (*Nigella sativa*) found in local markets, which contain their function in the phenols that comprise excess components and reductions of metal solutions from their salts and nitrates. 1 g of plant seeds (*N. sativa*) were crushed with an electric mixer, and the powder was put in a glass beaker with 100 ml of pure water free of mineral ions; it also contains pentacyclic soluble in water vegetable extract of plant seeds (*N. sativa*) found in local markets, which contain their function in the phenols that comprise excess components and reductions of metal solutions from their salts and nitrates. Plant seeds (*N. sativa*) of 1 gm were crushed using an electric mixer, and the powder was placed in a glass beaker (100 ml) of cleaned water devoid of mineral ions. Aqueous bismuth nitrate Bi(NO₃)₃ exists. It exists as colourless crystals (that as water).

Soluble and have a molecular weight of 395 g/mol and density of 2.8 gm/cm³. After weighing, 4.85 gm of bismuth nitrate using a delicate (4-digit) scale, it was dissolved in 100 mL of distilled wa-

ter, and the mixture was stirred by a magnetic stirrer at 80°C for 30 min with the addition of 3 mL acid HCl to complete the dissociation process.

We also obtained an aqueous solution of bismuth nitrate. Then, the plant extract of *Nigella sativa* was added gradually into the aqueous solution made of bismuth nitrate, and keep stirring with a magnetic stirrer to make it take on a new colour. The weight required for dissolution was calculated from nitrates of plant minerals to plant extracts using the following equation [9]:

$$M = (W_t/M_w) \cdot (1000/V). \quad (1)$$

Here, M is molar concentration, mol/L; W_t —solute weight, gm; W_t —molecular weight of, gm/mL; V —solvent volume, mL.

Figure 1 shows the mechanism of preparing bismuth oxide solution using green synthesis technology.

The Bi_2O_3 NPs solution was deposited using the drop casting method while heating the glass/PSi substrate to a temperature of (80°C). We drop three drops of the generated nano-bismuth-oxide solution on the glass slide of the electric heater connected to the digital thermocouple, and then place it on the heater for 30 minutes to allow the solution to precipitate fully. For example, with XRD, UV-Visible, FTIR, TEM, by comparing with the international atlas JCPDS, the material identification of the existence and appearance of nanoparticles was found. Figure 2 shows the deposition process using drop casting.

The process of synthesis of bismuth-oxide nanoparticles, important diagnostic tests, application as solar cells and measurement of their parameters can be elucidated.

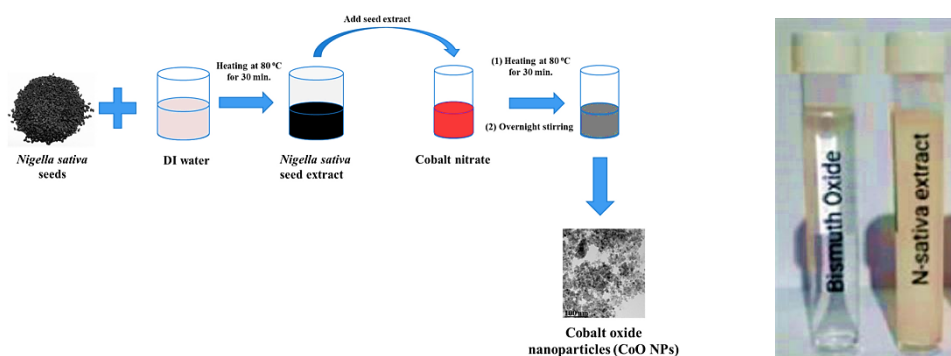


Fig. 1. Shows the mechanism of preparing bismuth oxide [19, 21].

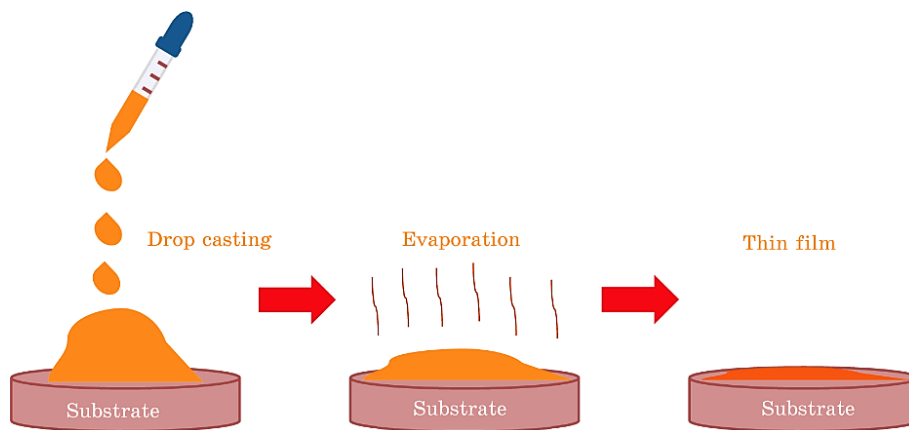


Fig. 2. The drop casting process [20, 21].

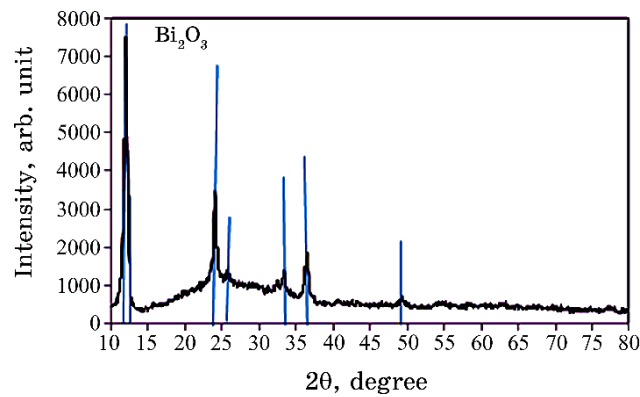


Fig. 3. XRD pattern of Bi_2O_3 thin film deposited by drop casting on glass [21].

4. RESULTS AND DISCUSSIONS

4.1. XRD

To examine the crystal structure of Bi_2O_3 film growth and to determine the nature of the crystal planes and their principal directions, x-ray diffraction patterns were used (the x-ray spectrum is shown in Fig. 3).

There are six distinct peaks corresponding to angles 25, 31, 39, 47, 54, 58, as shown in Table 1. They correspond to crystal planes (100), (101), (102), and (132), respectively. The deposited thin films show a tetragonal phase according to the cards numbers 00-050-1088, 00-044-1246 and 00-041-1449. This study approximates the

TABLE 1. The properties of (bulk) bismuth oxide Bi_2O_3 [21].

| Properties of materials | |
|-------------------------|--|
| Chemical symbol | Bi_2O_3 |
| Energy gap | 2.29–3.31 eV |
| Transmission | 375–542 nm |
| Colour | Yellow |
| Density | 8.9 g/cm ³ |
| Molar mass | 465.96 g/mol |
| Group | Bismuth 15/Oxygen 16 |
| Electron configuration | Bismuth ($[\text{Xe}]4f^{14}5d^{10}6s^26p^3$)/Oxygen ($[\text{He}]2s^22p^4$) |
| Melting point | 817°C |
| Boiling point | 1890°C |

TABLE 2. Result of inter planer for XRD pattern [21].

| $2\theta_{\text{std}}$, degree | $2\theta_{\text{exp}}$, degree | <i>hkl</i> planes | <i>d</i> -spacing, Å | <i>D</i> , nm | Strain, 10 ⁻⁴ | σ line/m ² , ×10 ¹⁴ | Card No. |
|---------------------------------|---------------------------------|-------------------|----------------------|---------------|--------------------------|--|--|
| 12.20 | 11.95 | (1 0 0) | 14.641 | 26.47 | 13.085 | 14.262 | Bi_2O_3 (00-050-1088) |
| 23.79 | 24.00 | (1 0 1) | 7.331 | 44.88 | 7.7204 | 4.9645 | Bi (00-044-1246) |
| 25.72 | 25.60 | (0 2 0) | 6.879 | 40.51 | 8.551 | 6.091 | Bi_2O_3 (00-041-1449) |
| 35.90 | 36.35 | (1 0 2) | 4.887 | 36.17 | 9.579 | 7.6428 | Bi_2O_3 (00-041-1449) |
| 49.43 | 49.10 | (1 3 2) | 3.669 | 41.40 | 8.369 | 5.834 | Bi_2O_3 (00-041-1449) |

findings by T. P. Gujar, V. R. Shinde, C. B. Lokhande, R. S. Mane, and S. H. Han (2005) [11], as shown in Table 2.

4.2. UV–VIS

The existence of Bi_2O_3 NPs was identified by examining the ultra-violet spectrum (UV–VIS).

It was also revealed that absorption was at $35 \cdot 10^4 \text{ cm}^{-1}$ while scanning at wavelengths spanning from 300 to 900 nm. In the photon energy range from 1 eV to 7 eV, the optical energy gap of Bi_2O_3

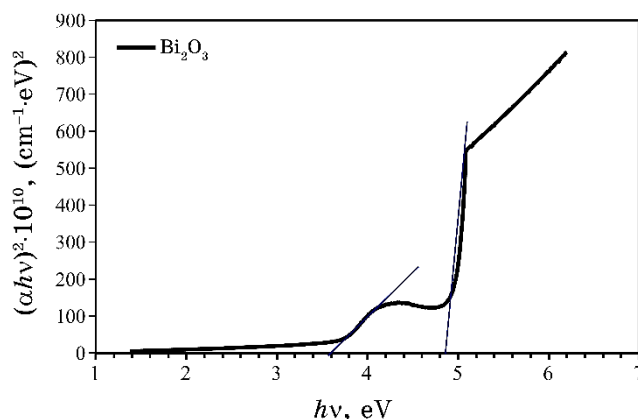


Fig. 4. Plot of $(\alpha hv)^2$ versus (hv) of Bi₂O₃ NPs film [21].

nanoparticles is $E_{g_1} = 3.6$ eV and $E_{g_2} = 4.9$ eV. This is accomplished by presenting magnitude $(\alpha hv)^2$ as a function of photon energy hv , as seen in Fig. 4.

The growing amount of the energy gap returns to the point when the matter transition into to a nanostate. The cause for the creation of two energy gaps for the same film is due to the fission of the Fermi level and the formation of new energy orders inside the previous energy gap. The absorption coefficient greater than $1 \cdot 10^4$ cm⁻¹ that mean the $r = 1/2$, and the electron transfers were of the direct type.

4.3. FTIR

Fourier spectroscopy was used as a diagnostic tool for the energy of effective bonds at the main absorption zones. FTIR spectrum of Bi₂O₃ solution, strong peak was centred at 3340.43 cm⁻¹, which is attributed to the presence of the hydroxyl radical adsorbed to the surface of the nanomaterial (O–H stretch), while the peak was at 1631.41 cm⁻¹, which represents the O–H scissors, while the bond was 738 cm⁻¹. The hydroxyl radical Bi–OH and the bond are 646.93 cm, 604.69 cm, and 604.69 cm⁻¹, respectively; so, it corresponds to the bonding of the produced metal oxide Bi–O.

Figure 5 displays the FTIR spectrum, peak locations, and active bonds of the prepared material, while Table 3 gives the results for the prepared material, namely, FTIR spectrum of Bi₂O₃ solution and bismuth oxide layers formed at a low reaction temperature.

These results are almost in agreement with the results obtained earlier by other researchers N. Motakef-Kazemi and M. Yaqoubi (2020) [12].

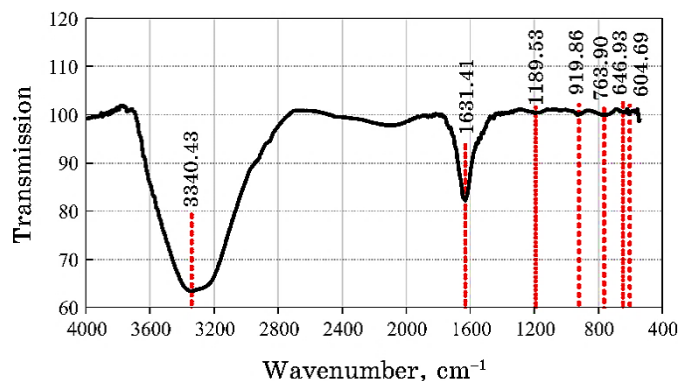


Fig. 5. FTIR measured for bismuth oxide thin film deposited on glass [21].

TABLE 3. FTIR assessment for Bi_2O_3 [21].

| Band Type | FTIR Assessment for (Bi_2O_3) |
|-----------|---|
| 3340.43 | O-H Stretch |
| 1631.41 | O-H Scissor |
| 1189.53 | Bi-OH |
| 919.86 | C-O |
| 763.90 | |
| 646.93 | Bi-O |
| 604.69 | |

4.4. SEM

Figure 6 displays pictures taken by a scanning electron microscope that are used to examine the surface topography of a thin film of Bi_2O_3 that has been applied to the surface of a glass slide. The images revealed a uniform distribution of small particles grouped into uniform groups covering the glass surface, along with nanocrystallite of various shapes and sizes, as well as acinus and nanoneedles with an average size of 70.1 nm.

These findings almost exactly match the researchers' findings (H. Shirkhanloo, M. Safari, S. M. Amini, and M. Rashidi (2017) [13]).

4.5. EDS

It was discovered that the elements are present in proper ratios by looking at their energy dispersion spectrometers. As illustrated in Fig. 7, the sample was coated with a small layer of gold to boost the reflectivity of the electronic beam falling vertically on the sample

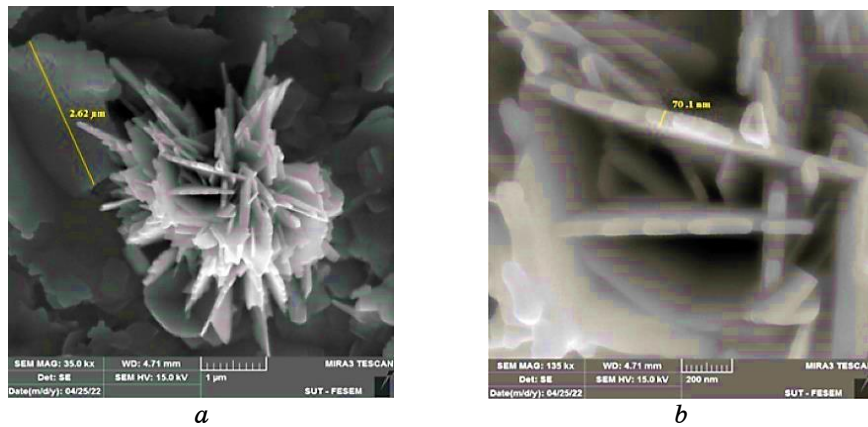


Fig. 6. SEM of Bi_2O_3 thin film preparing by drop casting method [21].

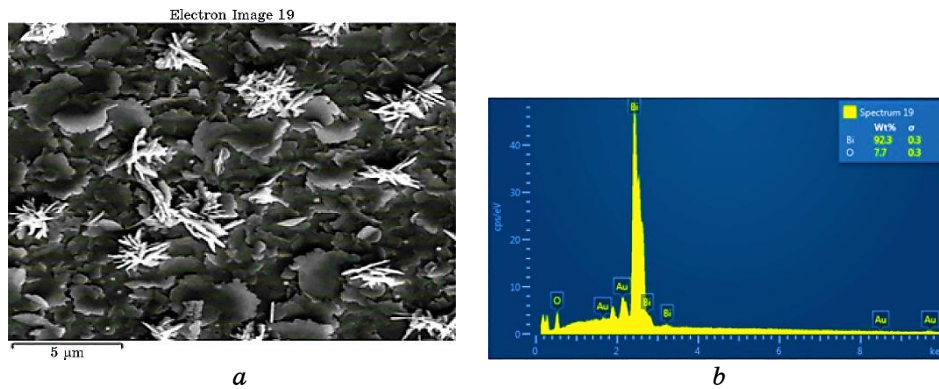


Fig. 7. EDS of Bi_2O_3 thin film preparing by drop casting method [21].

under examination. This caused the appearance of the gold element.

4.6. AFM

Since the atomic force microscope provides accurate information about the surface roughness and the nature of the particle distribution within the atomic grains as well as the root mean square of these grains by scanning the surface for films and at a temperature of 80°C , the surface topography of the deposited Bi_2O_3 films prepared by drop casting method was studied using the atomic force microscope (AFM).

The Bi_2O_3 NPs thin film is depicted in three dimensions in Fig. 8, as shown in Table 4.

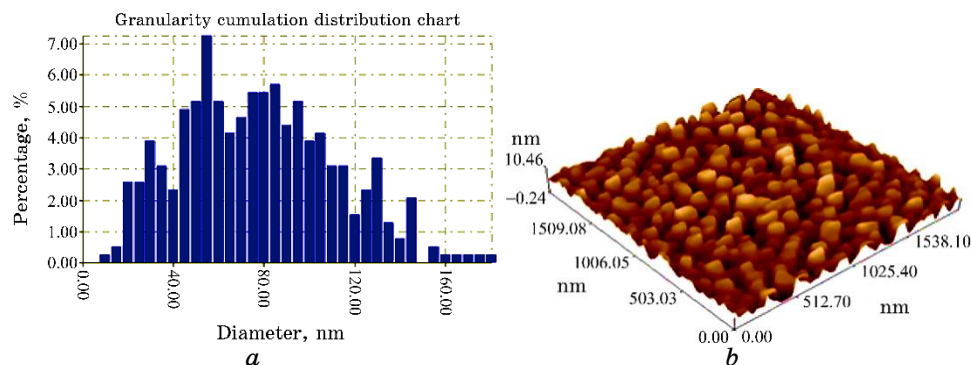


Fig. 8. AFM images of the topography of a pure Bi_2O_3 film deposited at 80°C [21].

TABLE 4. AFM data [21].

| Item B_2O_3 thin film | Average diameter size, nm | Roughness average, nm | Root mean square, nm |
|---------------------------------------|---------------------------|-----------------------|----------------------|
| $\text{Bi}_2\text{O}_3/\text{glass}$ | 95.03 | 1.50 | 1.57 |

4.7. $I-V$

In order to create the porous silicon PSi, electrochemical etching (ECE) was used. In order to stimulate the corrosion process, American-made silicon wafers (n -type > 100) with ohmic resistance 1–10 were used. Current density of 25 mA/cm^2 and effect time of 20 min were used under the illumination of a halogen lamp with a capacity of 70 W and at a vertical distance of 20 cm from the sample to be prepared. The silicon Si wafer serves as the cathode and a gold ring serves as the anode. The drop casting process was used to create the thin film for the solar cell $\text{Ag}/\text{Bi}_2\text{O}_3/\text{PSi}/\text{Si}/\text{Ag}$. The $I-V$ in dark and the $I-V$ lighted, filling factor (FF), and transformation efficiency are some of the most crucial electrical characteristics of a solar cell. A solar cell is a technology that efficiently converts light energy into electrical energy. One of the crucial electrical characteristics that illustrate how the current behaves with the voltage applied to the cell in the cases of forward and reverse bias is the $I-V$ property, which is used to describe the performance of heterojunction cells. Figure 9 illustrates the current–voltage characteristics (in dark) of the $\text{Ag}/\text{Bi}_2\text{O}_3/\text{PSi}/\text{Si}/\text{Ag}$ heterojunction prepared by drop casting technique.

Figure 10 shows that the current increases with the increase in voltage when the bias is forward, but when the bias is reverse, the

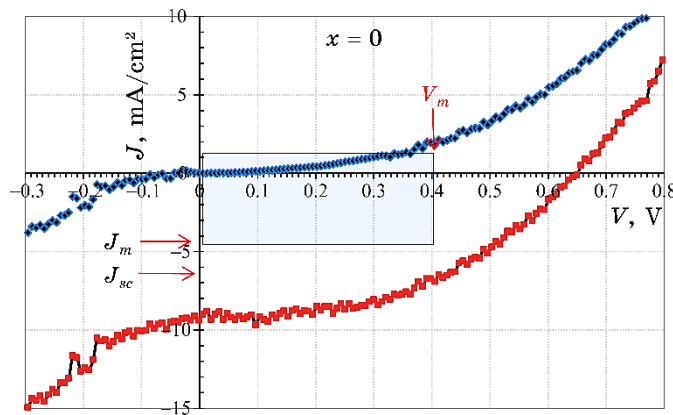


Fig. 9. *I*–*V* characteristics of Ag/Bi₂O₃/PSi//Si/Ag in illuminated and dark [21].

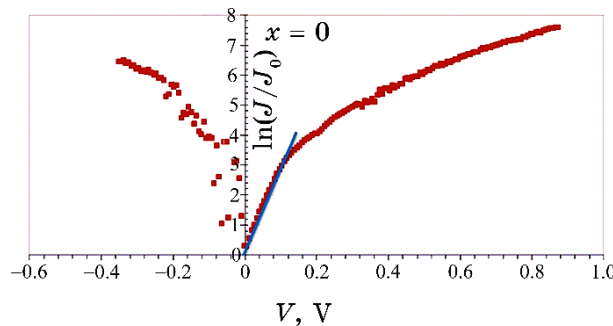


Fig. 10. Calculated ideality factor–*V* curve [21].

current increases gradually with the bias voltage and provides a gradual breakdown voltage. This behaviour is a general property of heterojunctions. When the bias is in the forward direction, the width of the depletion region narrows as the voltage rises. The majority of charge carriers are injected by the applied bias voltage in the forward bias state, which reduces the breadth of the depletion region and raises the concentration of the majority and minority carriers.

Due to the ability of establishing the parameters of the solar cell and measuring its conversion efficiency, the measurement of current–voltage characteristics in the condition of illumination is one of the most crucial measurements for solar cells. The solar cell was exposed to white light with intensity of 100 W/cm²; and by using the *I*–*V* relationship in the case of illumination, we can draw it as in Fig. 10 to show the change in values of the illumination current

as a function of the reverse bias voltage. Two tangents are drawn to acquire the parameters of the solar cell, and from their convergence, the maximum value of P_{\max} (maximum power point) is calculated.

4.8. Solar Cell Parameters

While the value of the short-circuit current I_{SC} was found at $V = 0$, where we extract the value of the output power from the product of the voltage and current, the open circuit voltage V_{SC} was determined at $I = 0$ and equal to $V_{OC} = 94$ mV. The filling factor was computed using the relationship (2) and the open circuit voltage and short circuit current ($P_{\text{out}} = V_{OC}I_{SC}$), and its result was $FF = 17.11436$. By dividing the current I_{SC} by the effective junction area A_{eff} in units of cm^2 ($J_{SC} = I_{SC}/A_{\text{eff}}$), the short-circuit current density is calculated to be $J_{SC} = 4$ mA/cm². The efficiency of the solar cell was determined to be = 2.8 using the preceding measurements and the calculation made in accordance with relationship (3). Calculating solar cell characteristics using equations [14, 15] were as follow:

$$FF = \left(\frac{P_{\max}}{V_{OC}I_{SC}} \right) \cdot 100\%, \quad (2)$$

$$\eta = \left(\frac{I_{SC}V_{OC}}{P_{in}} \right) \cdot FF. \quad (3)$$

Filling factor, maximum voltage for solar cells, maximum current density, maximum current in a short circuit, and maximum voltage in an open circuit are all represented by the letters FF , I_{SC} , and V_{OC} . The P_{in} represents the amount of energy dropping perpendicularly on a unit area over a unit time—radiation dose rate [16, 17].

4.9. Ideality Factor

The ideality factor β is calculated through the mathematical relationship (3) as the graphical relationship is drawn between the bias voltage on the x -axis and $\ln(J/J_0)$ on the y -axis. After finding the slope of the tangent to the curve, the reciprocal of the slope of the

TABLE 5. Solar cell parameter Ag/Bi₂O₃/PSi//Si/Ag in illuminated.

| V_{OC} , V | I_{SC} , mA | V_m , V | J_m , mA | R_w , m ² | FF | Eff., % | β | $R_{CH}(\Omega)$ | $R_S(\Omega)$ |
|--------------|---------------|-----------|------------|------------------------|------|---------|---------|------------------|---------------|
| 0.65 | 9.00 | 0.40 | 7.00 | 100 | 0.48 | 2.8 | 1.35 | 175 | 25.14 |

tangent is multiplied with the value $q/(k_B T)$.

The increase in the value of the ideality factor indicates that the re-joining current is dominant, and this is due to the presence of additional energy levels resulting from the deep defects in the polymorphic and shaped materials. Figure 10 illustrates the curve of the ideality factor [18]:

$$\beta = \frac{q}{k_B T} \frac{I_f}{\ln(I_f / I_S)}, \quad (3)$$

where k_B is Boltzmann constant, T —absolute temperature, I_f —forward bias current, I_S —saturation current.

5. CONCLUSIONS

Drop casting on glass substrates was used to describe the precipitated Bi₂O₃ films. Through optical investigations utilizing the visible and ultraviolet spectrum, two optical energy gaps, one in the visible spectrum and the other in the ultraviolet, were used with Tauc equation to determine the kind of transmission (direct transmission). Testing revealed that the green manufacturing of nanoparticles produced successful results.

REFERENCES

1. T. M. Joseph, D. Kar Mahapatra, A. Esmaeili, L. Piszczyk, M. S. Hasanin, M. Kattali, J. Haponiuk, and S. Thomas, *Nanomaterials*, **13**, No. 3: 574 (2023); <https://doi.org/10.3390/nano13030574>
2. C. L. Keat, A. Aziz, A. M. Eid, and N. A. Elmarzughi, *Bioresour. Bioprocess.*, **2**, No. 47: 1 (2015); [doi:10.1186/s40643-015-0076-2](https://doi.org/10.1186/s40643-015-0076-2)
3. Yejun Qiu, Jie Yu, Xiaosong Zhou, Cuili Tan, and Jing Yin, *Nanoscale Res. Lett.*, **4**: 173 (2009); <https://doi.org/10.1007/s11671-008-9221-6>
4. Zahrah Alhalili, *Molecules*, **28**, No. 7: 3086 (2023); <https://doi.org/10.3390/molecules28073086>
5. P. C. Nagajyothi, P. Muthuraman, T. V. M. Sreekanth, D. H. Kim, and J. Shim, *Arabian Journal of Chemistry*, **10**, No. 2: 215 (2017); <https://doi.org/10.1016/j.arabjc.2016.01.011>
6. L. Leontie, M. Caraman, M. Alexe, and C. Harnagea, *Surface Science*, **507–510**: 485 (2002); [https://doi.org/10.1016/S0039-6028\(02\)01289-X](https://doi.org/10.1016/S0039-6028(02)01289-X)
7. R. H. AL-Saqa and I. K. Jassim, *Digest Journal of Nanomaterials & Biostructures*, **18**, No. 1: 165 (2023); <https://doi.org/10.15251/DJNB.2023.181.165>
8. Simona Condurache-Bota, *Bismuth Oxide Thin Films for Optoelectronic, and Humidity Sensing Applications* (IntechOpen: 2018); [doi:10.5772/intechopen.75107](https://doi.org/10.5772/intechopen.75107)
9. X. Y. Chen, H. S. Huh, and S. W. Lee, *Journal of Solid State Chemistry*,

- 180, Iss. 9: 2510 (2007); <https://doi.org/10.1016/j.jssc.2007.06.030>
10. Z. Yang, S. Zhang, L. Li, and W. Chen, *Journal of Materiomics*, **3**, Iss. 4: 231 (2017); <https://doi.org/10.1016/j.jmat.2017.09.002>
 11. T. P. Gujar, V. R. Shinde, C. D. Lokhande, R. S. Mane, and S. H. Han, *Applied Surface Science*, **250**, Nos. 1–4: 161 (2005); <http://dx.doi.org/10.1016/j.apsusc.2004.12.050>
 12. N. Motakef-Kazemi and M. Yaqoubi, *Iranian Journal of Pharmaceutical Research (IJPR)*, **19**, No. 2: 70 (2020); <https://doi.org/10.22037/2Fijpr.2019.15578.13190>
 13. H. Shir Khanloo, M. Safari, S. M. Amini, and M. Rashidi, *Nanomedicine Research Journal*, **2**, No. 4: 230 (2017); <https://doi.org/10.22034/nmrj.2017.04.004>
 14. V. Badescu, *Comprehensive Renewable Energy* (Ed. M. Trevor Letcher) (Elsevier: 2022), p. 256–292; <https://doi.org/10.1016/B978-0-12-819727-1.00099-6>
 15. R. H. Al-Saqa, I. K. Jassim, and M. M. Uonis, *Ochrona przed Korozjq*, **66**, No. 8: 243 (2023); DOI: 10.15199/40.2023.8.3
 16. M. Rasheed, O. Y. Mohammed, S. Shihab, and Aqeel Al-Adili, *J. Phys.: Conf. Ser.*, **1795**: 012042 (2021); doi:10.1088/1742-6596/1795/1/012042
 17. S. S. Mali, P. Shinde, C. A. Betty, P. N. Bhosale, Y. W. Oh, and P. Patil, *Journal of Physics and Chemistry of Solids*, **73**, Iss. 6: 735 (2012); <https://doi.org/10.1016/j.jpcc.2012.01.008>
 18. H. B. Hassan, H. M. Abduljalil, and A. Hashim, *Nanosistemi, Nanomateriali, Nanotehnologii*, **21**, Iss. 2: 289 (2023); <https://doi.org/10.15407/nnn.21.02.289>
 19. Neha Sharma, Ankireddy Seshadri Reddy, and Kyusik Yun, *Chemosphere*, **32**: 131029 (2021); <https://doi.org/10.1016/j.chemosphere.2021.131029>
 20. Edward Bormashenko, Yelena Bormashenko, and Mark Frenke, *Materials*, **12**, Iss. 18: 3051 (2019); <https://doi.org/10.3390/ma12183051>
 21. H. H. Ahmed, A. M. Ali, and A. N. Abd, *Journal of Biomechanical Science and Engineering*, **3**: 179 (2023); doi:10.17605/OSF.IO/TF5AP; https://www.researchgate.net/publication/370480788_Bi2O3_NPs_BIOSYNTHESIS_CHARACTERIZATION_AND_USING_FOR_SOLAR_CELL_APPLICATION